Check for updates

Journal of the Optical Society of America B

OPTICAL PHYSICS

Converting the guided modes of Bloch surface waves with the surface pattern

Xi Tang,[1] **Haoqi Luo,**[1] **Junxue Chen,**[2,4] **Ramachandram Badugu,**[3] **Pei Wang,**[1] **Joseph R. Lakowicz,**[3] **and Douguo Zhang**[1,*]

[1]*Institute of Photonics, Department of Optics and Optical Engineering, University of Science and Technology of China, Hefei, Anhui, 230026, China*

[2]*College of Science, Guilin University of Technology, Guilin, Guangxi, 541004, China*

[3]*Center for Fluorescence Spectroscopy, Department of Biochemistry and Molecular Biology, University of Maryland School of Medicine, 725 West Lombard St., Baltimore, Maryland 21201, USA*

[4]*e-mail: cjxueoptics@glut.edu.cn*

*Corresponding author: dgzhang@ustc.edu.cn

The guided modes of Bloch surface waves, such as the transverse electric modes (TE00 and TE01 modes), can simultaneously exist in a low-refractive-index ridge waveguide with subwavelength thicknesses that are deposited on an all-dielectric one-dimensional photonic crystal. By using the finite-difference frequency-domain method, coupled mode theory, and the finite-difference time-domain method, the conversion between the guided modes has been investigated. This conversion can be realized in a broadband wavelength with the surface pattern of this low-index ridge. This conversion is useful for developing lab-on-a-chip photonic devices, such as a mode converter that can maintain the output mode purity over 90% with a working wavelength ranging from 590 to 680 nm, and a power splitter that can maintain the splitting ratio over 8:2 with a wavelength ranging from 530 to 710 nm.   © 2021 Optical Society of America

https://doi.org/10.1364/JOSAB.418106

1. INTRODUCTION

Device miniaturization is a major developmental direction of modern photonics and is of vital importance to optical communication and all-optical computations. High-density photonic integrated circuits (PICs) with nanophotonic devices have great potential in this field. Nanophotonic devices such as waveguides, beam splitters, and interferometers are key elements of PICs [1–6]. One way to realize these devices is to use the surface plasmon polaritons (SPPs) existing on the metallic nanostructures [7]. However, metal based on the property of materials will introduce ohmic loss, which will dramatically increase in the visible light band. On the other hand, all-dielectric photonic devices based on Bloch surface waves (BSWs) have been developed rapidly in the past several years; they have the merits of extremely low propagation loss compared with SPPs. BSWs are surface electromagnetic waves that exist at the interface between a truncated periodic dielectric multilayer and its surrounding medium [8]. This periodic dielectric multilayer is also called a one-dimensional photonic crystal (1DPC) that has a photonic bandgap (PBG). The 1DPC can consist of different dielectric materials and dimensions, which makes it possible to realize either TE- or TM-polarized BSWs [9]. BSWs can be effectively excited over a wide wavelength range, propagate over several

millimeters and even up to centimeters, and also have the ability to enhance surface field [10]. Thus, BSWs have been widely adopted in the fields of sensing, enhanced Raman scattering, fluorescence emission, nonlinear optical effect, etc. [11–15]. All these features of BSWs over a 1DPC substrate are suitable for developing nanophotonic devices [16–20]. Recently, vortex beam generation with BSWs has been reported [21]. In addition, beam splitters, phase shifters, and Mach–Zehnder interferometers based on BSWs were successfully realized using the multimode interference (MMI) effect, where a dielectric ridge was fabricated on a 1DPC substrate (it can be called a dielectric-ridge-1DPC platform) [22]. However, to the best of our knowledge, there is no report on how to convert the guided BSW [23,24] modes loaded on the dielectric-ridge-1DPC platform.

In this paper, we demonstrate the conversion between guided modes of BSWs, which can be realized by introducing the surface pattern on the dielectric ridge. First, the finite-difference frequency-domain (FDFD) method [25] is used to prove the existence of multiple guided modes of BSWs in a dielectric ridge fabricated on the 1DPC. Second, based on the fact that the surface pattern will induce mode coupling, the coupled mode theory (CMT) [26] and finite difference time-domain (FDTD) method [27] are used to demonstrate the process of
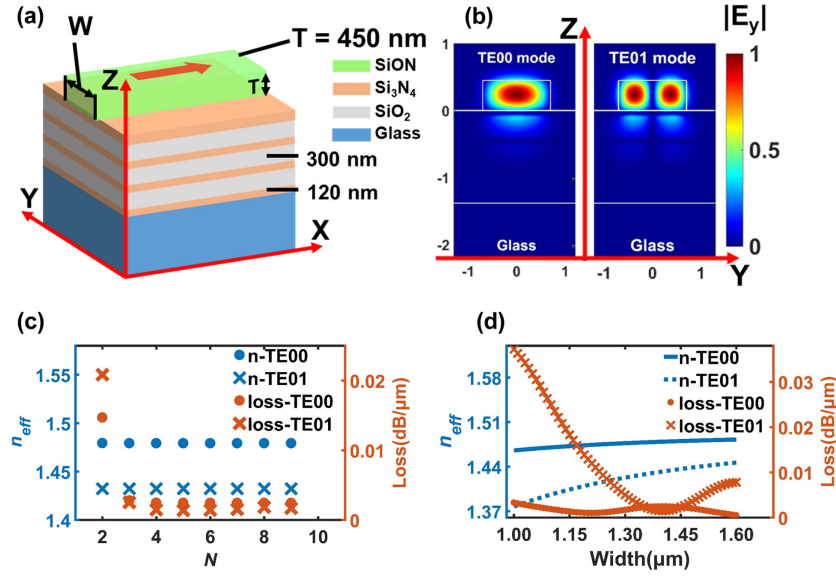
Fig. 1. (a) Schematic diagram of the dielectric-ridge-1DPC platform. The red arrow indicates the propagating direction. (b) The normalized electric field (E_y) amplitude distribution of the TE00 and TE01 modes. (c),(d) Effective refractive index (n_{eff}) and propagation loss as a function of the number of periods (N) and the ridge width (W).

mode conversion. At last, taking advantages of the mode conversion, a broadband mode converter and power splitter were demonstrated with the dielectric-ridge-1DPC platform.

The paper is organized as follows: in Section 2, we discuss the properties of guided BSWs, present the model of the refractive index surface pattern and structural surface pattern, show the results about the process of mode conversion with CMT and FDTD, and design the mode converter and power splitter to verify the possibility of integrating photonic devices on the 1DPC platform. In Section 3, we present our conclusions.

2. RESULTS AND DISCUSSION

A. Guided Modes of Bloch Surface Waves

The 1DPC is made up of four pairs of alternative dielectric layers of SiO_2 and Si_3N_4 except that the top SiO_2 layer is replaced by a dielectric ridge of finite width and thickness (dielectric-ridge-1DPC platform), as shown in Fig. 1(a). The refractive indices of Si_3N_4, SiO_2, and glass substrate are 2.650, 1.480, and 1.515, respectively. The thicknesses of the Si_3N_4 and SiO_2 are 120 nm and 300 nm, respectively. This dielectric ridge can be made of silicon oxynitride (SiON) film whose refractive index can be tuned for various applications, and in the following simulations and calculation, its refractive index was set at 1.590. The width and thickness of this dielectric ridge are denoted as W and T, respectively. This kind of BSW loaded on the dielectric-ridge-1DPC platform is called a guided BSW, which propagates only inside the top dielectric ridges [16,23].

When the thickness (T) and width (W) of the SiON ridge were fixed at 450 nm and 1.4 μm, the working wavelength was fixed at 633 nm and the number of periods (N) was four. The spatial distributions of the normalized electric field (E_y) amplitude of the two lowest-order BSW guided modes (TE00 and TE01 modes) were simulated with the FDFD method, as shown in Fig. 1(b). These simulations verify the existence of multiple

guided BSWs on the dielectric-ridge-1DPC platform, such as the TE00 and TE01 modes.

It can be anticipated that the properties of the guided BSWs loaded on the dielectric-ridge-1DPC platform depend on the geometrical parameters of 1DPC as well as the ridge thickness and width. The effective refractive indices ($n_{eff} = \mathrm{Re}(k_x/k_0)$) and the propagation loss (loss $= 10\log_{10}(\exp(-2\mathrm{Im}(k_x)))$) of the two guided BSWs as a function of the number of periods (N) were calculated by FDFD, as shown in Fig. 1(c). The propagation loss decreases rapidly with N increasing until $N = 4$, while the effective refractive index is almost invariant.

Then, when the number of multilayers was fixed ($N = 4$), the effective refractive indices of the guided BSWs increase as the width (W) of the ridge varied from 1 to 1.6 μm. But the propagation loss is not monotonic as the width decreases. The propagation loss has a local maximum for the TE00 mode while a local minimum for the TE01 mode at $W = 1.4$ μm. These simulation results show that the propagation distance and effective refractive indices of the guided BSWs can be controlled by the ridge width.

The influence of the working frequency on the propagation constant of the guided BSWs was also investigated. Figure 2(a) shows the photonic band structure of the 1DPC. The regions with gray color denote the forbidden bands of the 1DPC. The dispersion curves for the TE00 and TE01 modes with the ridge width $W = 1.4$ μm are shown with brown and blue solid lines, respectively. The two black solid lines are the light lines in vacuum (air) and homogeneous silica (SiO_2). The two red dashed lines indicate the wavelength range from 560 to 710 nm used in this paper. In this case, the guided BSWs are completely inside the PBG, which means the longitudinal leakage can be controlled effectively. Moreover, Fig. 2(b) shows the propagation loss of two modes as a function of working frequency. The black circle represents the working wavelength 633 nm. The loss for the TE01 mode can be minimum when the working
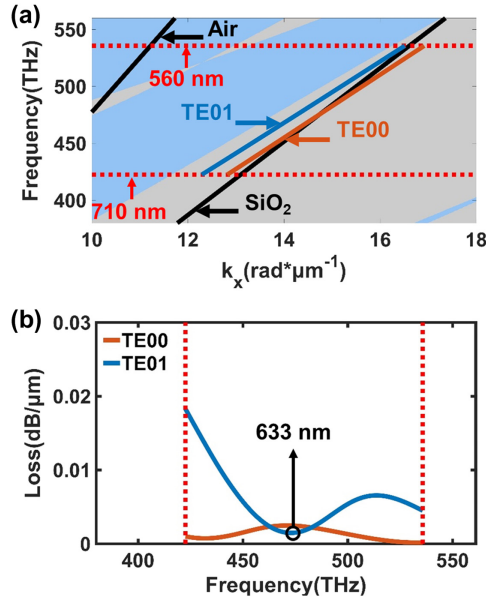
Fig. 2. (a) Photonic band structure of 1DPC and the dispersion relations of the guided BSWs. The forbidden band regions of the structure are denoted by gray color and the allowed band regions are denoted by blue color. (b) The propagation loss versus working frequency. The black circle points out the working wavelength used in the next section.

Table 1. Effective Refractive Index and Propagation Loss of Guided BSWs

	TE00	TE01	TE02	TM00	TM01
Re (n_{eff})	1.4792	1.4323	1.3541	1.4767	1.4386
Im (n_{eff})	2.8563e-5	1.7222e-5	5.9807e-5	5.5626e-4	7.5959e-4
Loss (dB/μm)	0.0025	0.0015	0.0516	0.0480	0.0655

wavelength is 633 nm. Then, the optimized parameters of the dielectric-ridge-1DPC platform can be selected as $W = 1.4$ μm, $T = 450$ nm, and $N = 4$ to realize the guided BSWs. In Table 1, we show the effective refractive indices and propagation loss of guided BSWs. All effective refractive indices are lower than the refractive index of the glass substrate, which cannot exist when the substrate is only glass. This special feature means the guided BSW is no longer limited by the refractive of structure substrate and shows the potential value in PICs. And the propagation losses of the TE00 and TE01 modes are much lower than other modes. So the two lowest orders of guided BSWs with extreme low propagation loss will be used for the following demonstrations of mode conversion from the TE00 mode to the TE01 mode.

B. Converting the Guided Modes of Bloch Surface Waves

In this section, we will investigate the mode conversion with specific perturbation distribution by the CMT at first. And then, we will demonstrate how to design the structural surface pattern for realizing the mode conversion by using the 3D-FDTD method. The working wavelength is set at 633 nm.

In the CMT, we ignore the time harmonic term, $\exp(j\omega t)$, and losses of the two lowest-order modes first, and then the coupled mode equations used for the two modes can be given as [2,26]

$$\frac{dA_0}{dx} = -jK_{00}(x)A_0 - jK_{01}(x)A_1 \exp[j(k_{x0} - k_{x1})x],$$

$$\frac{dA_1}{dx} = jK_{11}(x)A_1 - jK_{10}(x)A_0 \exp[-j(k_{x0} - k_{x1})x],$$

$$\tag{1}$$

where A_0 and A_1 are the complex amplitudes of the TE00 and TE01 modes, respectively. K_{00} and K_{11} are the mode self-coupling coefficients. K_{01} and K_{10} are the mutual coupling coefficients between the TE00 and TE01 modes. k_{x0} and k_{x1} are the propagating constants of the TE00 and TE01 modes, respectively. The coupling coefficient can be described as

$$K_{pq}(x) = \frac{\omega\varepsilon_0}{4} \iint_S \Delta\varepsilon(x, y, z) E_p^*(y, z) E_q(y, z)\mathrm{d}y\,\mathrm{d}z, \tag{2}$$

where the subscripts p and q indicate the two modes. $E_p(y, z)$ or $E_q(y, z)$ means the electric field of the TE00 mode if p or $q = 0$; $E_p(y, z)$ or $E_q(y, z)$ means the electric field of the TE01 mode if p or $q = 1$. S is the cross section of the ridge and $\Delta\varepsilon$ is the surface pattern distribution in the ridge waveguide. ω is the angular frequency and ε_0 is the vacuum permittivity.

For the CMT, the key point is how to describe the spatial distribution of perturbation inside the dielectric ridge. We assume the refractive index distribution of perturbation is formed by the interference between the TE00 and TE01 modes, whose spatial distribution $\tilde{n}(x, y, z)$ can be described by Eq. (3). The term c.c means the complex conjugate of the second term of Eq. (3). n_0 represents the unperturbed part of the refractive index ($n_0 = 1.590$ here) and $\Delta n(y, z)$ represents the perturbation distribution in the $Y-Z$ plane. Similar to [2], we calculated the theoretical refractive index distribution of perturbation $\Delta n(y, z)$ with Eq. (4). Δn_{max} is the maximal index modulation factor. $E_y^{TE00}(y, z = z_0)$ and $E_y^{TE01}(y, z = z_0)$ are the unperturbed normalized electric-field (E_y) distribution of the TE00 and TE01 modes at the middle of the dielectric waveguide (in the vertical direction, $z_0 = 225$ nm), respectively. These fields are extracted from the cross section of the ridge waveguide, as shown in Fig. 1(b). Since the $\hat{y}$ components of the electric fields are identical for the TE00 and TE01 modes in the vertical direction, $\Delta n(y, z)$ is uniform along the Z axis. This feature makes it simpler for calculating the curve of mode conversion. We choose $\Delta n_{max} = 0.0197$ as the perturbation factor, and the core refractive index n_0 is set as 1.590 to avoid self-coupling of the mode.

To calculate the coupling coefficient through Eq. (2), Eq. (5) is used to calculate the perturbation distribution $\Delta\varepsilon(x, y, z)$. The higher-order perturbation term $\Delta n(x, y, z)^2$ is ignored. This perturbation distribution will induce the mode conversion as the guided BSWs propagates across this region:

$$\tilde{n}(x, y, z) = n_0 + \Delta n(x, y, z) = n_0 + \Delta n(y, z)$$

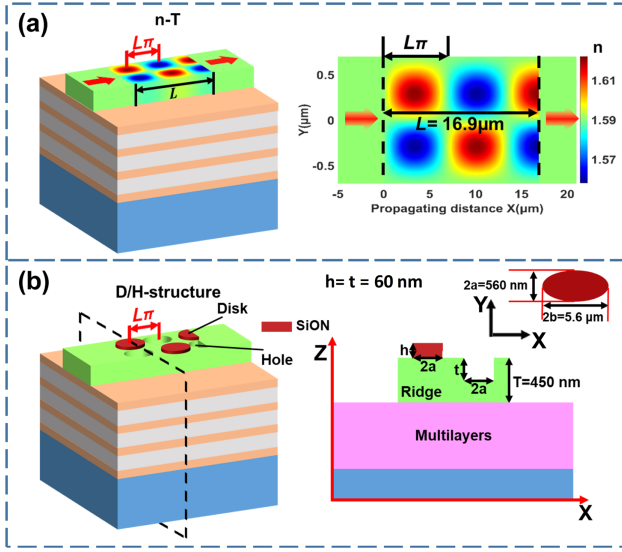$$\times \exp[j(k_{xm} - k_{xn})x] + \text{c.c}, \tag{3}$$

Fig. 3. Schematic diagram of the ridge waveguide with (a) refractive index surface pattern ($n-T$) or (b) structural surface pattern (D/H structure).

$$\Delta n(y, z) = \Delta n_{\max}[E_y^{\text{TE00}}(y, z = z_0)]^* E_y^{\text{TE01}}(y, z = z_0), \quad (4)$$

$$\Delta\varepsilon(x, y, z) = \tilde{\varepsilon}(x, y, z) - \varepsilon(x, y, z)$$
$$= \tilde{n}(x, y, z)^2 - n_0^2 \approx 2n_0\Delta n(x, y, z). \quad (5)$$

Figure 3(a) shows the refractive index surface pattern ($n - T$) on the ridge in the $Y-Z$ plane as described in Eq. (3). The length of this region is defined as L along the X axis. This length also can be called the coupling distance (L) because the mode conversion or mode coupling happens in this perturbed area. In the right side of Fig. 3(a), the refractive index distribution in the $X-Y$ plane was pictured when L was chosen as 16.9 μm. Taking Eq. (5) into Eq. (2), we could find that the coupling coefficient (K_{01}) shown in Eq. (6) is related to the integral of the perturbation or refractive index distribution. Due to the antisymmetric refractive index distribution along the transverse direction (Y axis) in Fig. 3(a), the self-coupling coefficients K_{00} and K_{11} coming from Eq. (2) are zero for the refractive index surface pattern ($n-T$):

$$K_{01}(x) = \frac{\omega\varepsilon_0}{4}\iint_S 2n_0\Delta n(x, y, z)E_0^*(y, z)E_1(y, z)\mathrm{d}y\,\mathrm{d}z. \quad (6)$$

In fact, acquiring $n-T$ is highly challenging, so the aim of using $n-T$ is to obtain the K_{01} as a function of coupling distance (L). And it is important to explore an effective structure to acquire the same functionality. We define a parameter called C_{eq}, which is the integral of K_{01} from $X = 0$ to $X = L_\pi$ along the X axis. This parameter helps us to design the structural surface pattern or perturbations, D/H structure (disks and holes fabricated on the ridge) shown in Fig. 3(b). The elliptic disks and holes are of the same geometric parameters in the $X-Y$ plane, where the lengths of the short axis (a) and long axis (b) are 280 nm and 2.80 μm, respectively. The height (h) of the disks and the depth (t) of holes are both 60 nm, which may be fabricated by electron beam lithography [28,29] and focused ion
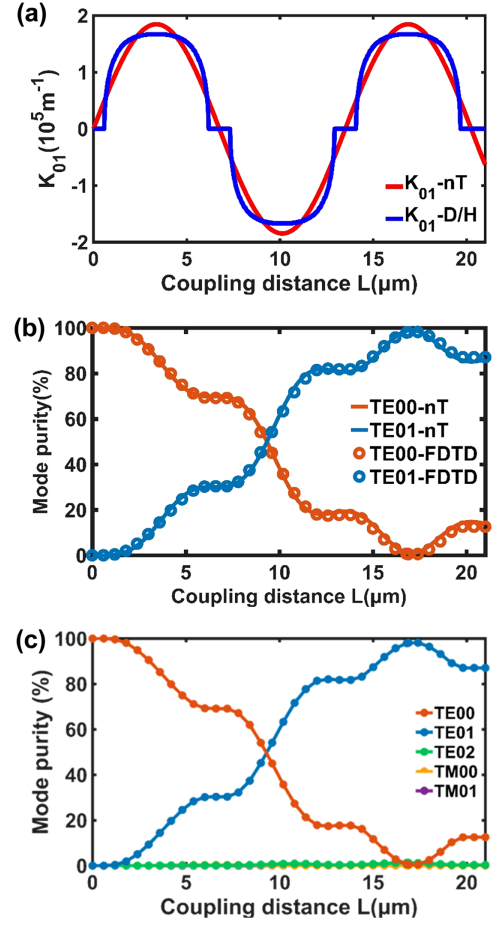

Fig. 4. Mode conversion between the guided BSWs. (a) Calculated K_{01} versus coupling distance L. The red line corresponds to the refractive index surface pattern and the blue line corresponds to the structural surface pattern. (b) The curves of mode purity calculated by CMT with $n-T$ and FDTD with D/H structure. (c) The mode purity of all five guided BSWs as a function of coupling distance L.

beam [30–32]. In this structure, it is not antisymmetric completely and the self-coupling coefficient is not zero, but it can be negligible when comparing with mutual-coupling coefficient K_{01}. Figure 4(a) presents the curve of mutual-coupling coefficient K_{01} as a function of the coupling distance (L) obtained from Eq. (6). The C_{eq} of $n-T$ and D/H structure are equal to each other, so the refractive index surface pattern can be realized by the D/H structure:

$$C_{\text{eq}} = \int_0^{L_\pi} K_{01}(x)\mathrm{d}x, \quad (7)$$

$$L_\pi = \frac{\pi}{k_{x0} - k_{x1}}. \quad (8)$$

To quantify and verify the mode conversion from the TE00 to TE01 modes, 3D-FDTD is used to calculate the electric field and the field is decomposed into the eigenmodes to acquire the power transmission of each mode at the output port. Because it is hard to separate scattering loss from the structural surface pattern in 3D-FDTD, we should ignore the influence of any loss when comparing the results calculated by FDTD with that by the CMT. Mode purity is defined as the ratio between

the power of the output TE00 (or TE01) mode and the total output power, which reflects the ability of this photonic device to convert the TE00 to the TE01 mode. Figure 4(b) presents the curves of the mode conversion from TE00 to TE01 as a function of the coupling distance (L). The solid lines are obtained by the numerical solutions of CMT, and the hollow dots indicate the simulated data from the 3D-FDTD solution. These results agree well with each other but there are a few differences due to the cross talk of other modes. In Fig. 4(c), the curves of all five modes are presented. For example, the mode purity of all five modes are 0.50%, 98.11%, 1.30%, 0.07%, and 0.03%, respectively, when L is equal to 16.9 μm. These results verify that the mode conversion can happen with the designed surface pattern, as shown in Figs. 3(a) and 3(b).

C. Photonics Device Based on a Dielectric-Ridge-1DPC Platform

1. Broadband Mode Converter

In this section, we demonstrated that the designed mode converter (D/H structure) can work in a broadband wavelength and keep high purity of the output TE01 mode. The geometrical parameters of this structure are the same as that in Fig. 3(b). As an example, Fig. 5(a) presents the real part of the electric field (E_y) propagating along the ridge with the coupling area (D/H structure) is of 16.9 μm length (from $X = 0$ μm to $X = 16.9$ μm). The inset graph is the enlarged image of the region marked with a red dashed circle. The distribution of the electric field shown in the inset graph is antisymmetric with almost the same amplitudes (the characteristic of the TE01 mode). It is clearly verified that the input TE00 mode (at $X = 0$ μm) has been mainly converted to the TE01 mode with the structural pattern shown in Fig. 3(b) and the high purity TE01 mode could be acquired at the observation plane ($X = 29$ μm).

To quantify the loss coming from the D/H structure, the new parameter called transmittance is defined as the ratio between the total output power and the total input power. Transmittance can be used to indicate the transmission efficiency of the device. Figure 5(b) shows the curves of mode purity and transmittance versus working wavelength. The mode purity of the output mode can be larger than 90% when the wavelength varies from 590 to 680 nm, meaning that this device can work as a broadband mode converter. When the wavelength is 633 nm, transmittance is 91.9% at $X = 29$ μm.

Because the transmittance is 91.9%, the total loss including propagation loss and scattering loss is 8.1%. Equation (9) is used to calculate the energy loss due to the propagation loss of any pure mode. Here, we set T_{in} as 1 and $x = 29$ μm. When we only considered the propagation loss of the TE00 and TE01 modes, the T_{loss} is 1.63% and 0.99% of pure TE00 and TE01 modes and the scattering loss of the D/H structure is from 6.47%–7.11%:

$$T_{loss} = T_{in} \left\{ 1 - \exp[-2\mathrm{Im}(n_{eff})k_0 x] \right\}. \qquad (9)$$
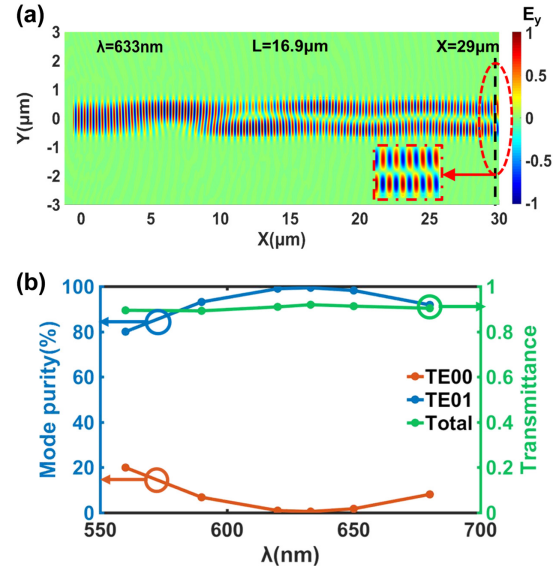

Fig. 5. Mode converter working in a broadband wavelength. (a) The electric field (E_y) distribution of the guided BSWs with working wavelength 633 nm. The inset is the magnified view of the region marked by a red dashed circle. The black dashed line at $X = 29$ μm indicates the position of the observation plane for calculating the mode purity. (b) The mode purity of the guided BSWs and total transmittance as a function of working wavelength.

2. Broadband Power Splitter

In this section, the partial mode conversion was used to realize the beam splitting and routing of the guided BSWs. First of all, we study the straight ridge waveguide with only one pair of disk and hole. The MMI effect would be used to clarify the splitting mechanism. And then, to obtain a power splitter in the 1DPC platform, a Y-branched ridge waveguide is used to replace straight ridge waveguide. Finally, we would discuss the broadband feature of this power splitter.

Figure 6(a1) shows the structure of the straight ridge with one pair of disk and hole. When the TE00 mode is launched in the waveguide, a part of the TE00 mode would be converted to the TE01 mode after passing through the perturbed region and the final interference pattern is formed due to MMI. From Fig. 4(c), the mode purity of the TE00 and TE01 modes is 69.16% and 30.34% when only one pair of disk and hole was used. Figure 6(a2) shows simulation of mode evolution when light propagates from left to right through the D/H structure at the center of the ridge waveguide. The asymmetric distribution of optical power makes it possible for designing the power splitter. In addition, the total transmittance is 97.04%, which means the scattering loss of the surface pattern is lower than 2.96%.

Based on the results shown before, the Y-branched waveguide is used to replace the straight waveguide. In Figs. 6(b1), 6(c1), and 6(d1), the schematic diagrams of the Y-branched waveguide with or without the structural surface pattern are presented. W_1 is defined as the input port, and W_2 and W_3 are the output ports. All the structural parameters are the same as those used before, except that the widths of two output arms of the Y-branches (W_2 and W_3) are 710 nm. The TE00 mode is excited at $X = 0$ μm. The splitting and routing of a beam with the structural surface pattern are shown in Figs. 6(b2), 6(c2), and 6(d2). We can find
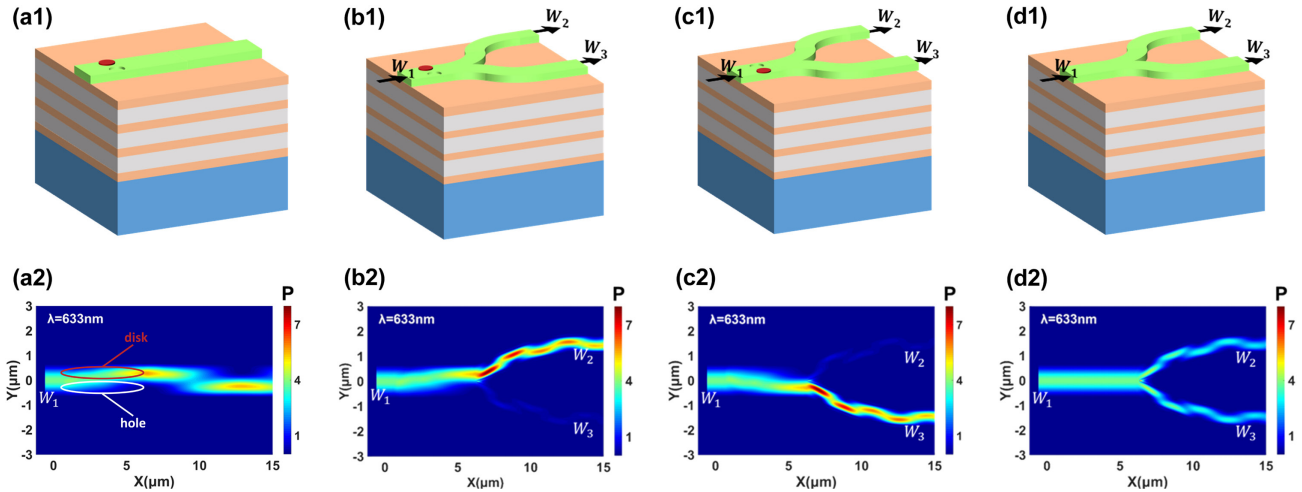
Fig. 6.   (a1) Structural surface pattern used for partial mode conversion. (b1)–(d1) Y-branches waveguide with or without the structural surface pattern as different power splitter. (a2)–(d2) Spatial magnitude distribution of the Poynting vector of the guided BSWs when the working wavelength is set at 633 nm. $W_1 = 1.4\ \mu m$, $W_2 = W_3 = 710$ nm. In (a2), the red and white circles indicate the positions of disk and hole.
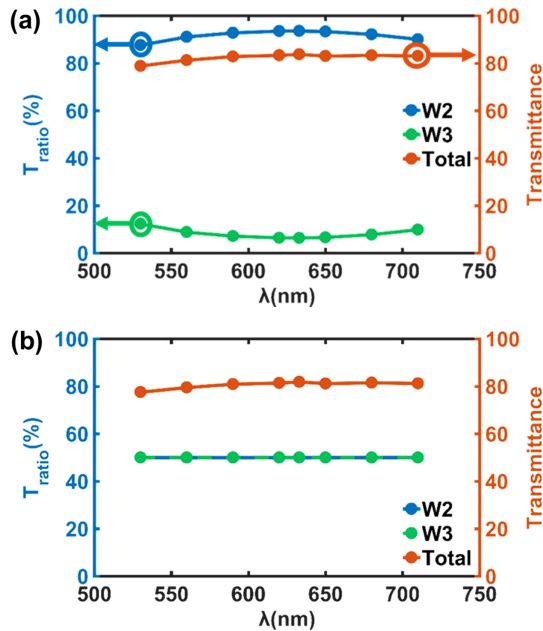

Fig. 7.   Transmittance spectra of the guided BSWs along the Y-branch waveguide. (a) 8:2 power splitter with the surface pattern shown in Fig. 6(b). (b) 5:5 power splitter without the surface pattern shown in Fig. 6(d). The blue line represents the ratio of transmittance flowing into port W_2, while the green line is for port W_3. The orange line indicates the total transmittance from W_2 and W_3.

that optical power mainly flows into the port W_2 as shown in Fig. 6(b2); meanwhile, optical power mainly flows into the port W_3 as shown in Fig. 6(c2). On the contrary, when there is no structural surface pattern [Fig. 6(d1)], the output power of ports W_2 and W_3 is the same, meaning a power splitting ratio of 5:5 [Fig. 6(d2)].

In Fig. 7, we detected the ratio of transmission and transmittance passing through the entire structure. The power splitting can be quantitatively described with the parameters $T_{ratio} = T_{W2}/T_{total}$ or T_{W3}/T_{total}. The curves of W_2, W_3,

and transmittance versus the working wavelength were calculated with the FDTD method, as shown in Figs. 7(a) and 7(b). For both devices, the transmittance is almost the same from 560 to 710 nm, which means the loss mainly comes from the Y-branches and the scattering loss of the surface pattern can be ignored. In addition, the results of Figs. 7(a) and 7(b) correspond to the structure shown in Figs. 6(b) and 6(d). The designed device with the surface pattern shown in Fig. 6(b) could work as the power splitter in a broadband wavelength, such as a high splitting ratio over 8:2 from 560 to 710 nm [Fig. 7(a)].

These results demonstrate that the surface pattern on the ridges can be used to tune the splitting ratio of this integrated power splitter, and flow direction of the guided BSWs which can be routed to the selected branch when working in the broadband wavelength. The mechanism for this splitter is due to the existence of mode conversion happening in the surface pattern and the MMI effect, as shown in Fig. 6.

3. CONCLUSIONS

In summary, we demonstrated that a low-refractive-index ridge waveguide placed on a 1DPC can sustain guided BSWs of different orders. Both numerical solutions of CMT and simulated results calculated by FDTD show that when the surface pattern was properly designed on this ridge, one guided BSW mode inside the ridge can be converted partially or mainly to another, just depending on the length of the perturbed region. The device designed for the high purity TE01 mode can be used as a mode converter. Due to the different spatial distribution of the different order guided BSW modes, the partial mode transformation will change the electric-field distribution inside the ridge, which can be used to develop the power splitter with various splitting ratios. Thus, our work provides a method on how to control the electromagnetic-field flow of the BSWs along a ridge, which will find applications in the integrated optics, such as developing elements for photonic-integrated-circuits or lab-on-a-chip devices for optical imaging and sensing [33,34].

Disclosures. The authors declare no conflicts of interest.

Data Availability. Data underlying the results presented in this paper are not publicly available at this time but may be obtained from the authors upon reasonable request.

REFERENCES

1. Z. Li, M. H. Kim, C. Wang, Z. Han, S. Shrestha, A. C. Overvig, M. Lu, A. Stein, A. M. Agarwal, M. Loncar, and N. Yu, "Controlling propagation and coupling of waveguide modes using phase-gradient metasurfaces," Nat. Nanotechnol. **12**, 675–683 (2017).

2. D. Ohana and U. Levy, "Mode conversion based on dielectric metamaterial in silicon," Opt. Express **22**, 27617–27631 (2014).

3. H. Wang, Y. Zhang, Y. He, Q. Zhu, L. Sun, and Y. Su, "Compact silicon waveguide mode converter employing dielectric metasurface structure," Adv. Opt. Mater. **7**, 1801191 (2018).

4. C. Yao, S. C. Singh, M. ElKabbash, J. Zhang, H. Lu, and C. Guo, "Quasi-rhombus metasurfaces as multimode interference couplers for controlling the propagation of modes in dielectric-loaded waveguides," Opt. Lett. **44**, 1654–1657 (2019).

5. P. Cheben, R. Halir, J. H. Schmid, H. A. Atwater, and D. R. Smith, "Subwavelength integrated photonics," Nature **560**, 565–572 (2018).

6. A. Bogdanov, K. Koshelev, P. Kapitanova, M. Rybin, S. Gladyshev, Z. Sadrieva, K. Samusev, Y. Kivshar, and M. Limonov, "Bound states in the continuum and Fano resonances in the strong mode coupling regime," Adv. Photonics **1**, 016001 (2019).

7. W. L. Barnes, A. Dereux, and T. W. Ebbsen, "Surface plasmon subwavelength optics," Nature **424**, 824–830 (2003).

8. P. Yeh, A. Yariv, and C.-S. Hong, "Electromagnetic propagation in periodic stratified media. I. General theory*," J. Opt. Soc. Am. **67**, 423–438 (1977).

9. J. Chen, D. Zhang, P. Wang, H. Ming, and J. R. Lakowicz, "Strong polarization transformation of Bloch surface waves," Phys. Rev. Appl. **9**, 024008 (2018).

10. D. Aurelio and M. Liscidini, "Electromagnetic field enhancement in Bloch surface waves," Phys. Rev. B **96**, 045308 (2017).

11. A. L. Lereu, M. Zerrad, A. Passian, and C. Amra, "Surface plasmons and Bloch surface waves: Towards optimized ultra-sensitive optical sensors," Appl. Phys. Lett. **111**, 011107 (2017).

12. R. Rizzo, M. Alvaro, N. Danz, L. Napione, E. Descrovi, S. Schmieder, A. Sinibaldi, R. Chandrawati, S. Rana, P. Munzert, T. Schubert, E. Maillart, A. Anopchenko, P. Rivolo, A. Mascioletti, F. Sonntag, M. M. Stevens, F. Bussolino, and F. Michelotti, "Bloch surface wave label-free and fluorescence platform for the detection of VEGF biomarker in biological matrices," Sens. Actuators, B **255**, 2143–2150 (2018).

13. Y. H. Li, T. L. Yang, S. M. Song, Z. Y. Pang, G. Q. Du, and S. H. Han, "Phase properties of Bloch surface waves and their sensing applications," Appl. Phys. Lett. **103**, 041116 (2013).

14. A. Angelini, E. Enrico, N. De Leo, P. Munzert, L. Boarino, F. Michelotti, F. Giorgis, and E. Descrovi, "Fluorescence diffraction assisted by Bloch surface waves on a one-dimensional photonic crystal," New J. Phys. **15**, 073002 (2013).

15. R. Badugu, J. Mao, S. Blair, D. Zhang, E. Descrovi, A. Angelini, Y. Huo, and J. R. Lakowicz, "Bloch surface wave-coupled emission at ultra-violet wavelengths," J. Phys. Chem. C **120**, 28727–28734 (2016).

16. E. Descrovi, T. Sfez, M. Quaglio, D. Brunazzo, L. Dominici, F. Michelotti, H. P. Herzig, O. J. Martin, and F. Giorgis, "Guided Bloch surface waves on ultrathin polymeric ridges," Nano Lett. **10**, 2087–2091 (2010).

17. T. Sfez, E. Descrovi, L. Yu, M. Quaglio, L. Dominici, W. Nakagawa, F. Michelotti, F. Giorgis, and H. P. Herzig, "Two-dimensional optics on silicon nitride multilayer: Refraction of Bloch surface waves," Appl. Phys. Lett. **96**, 151101 (2010).

18. Y. Augenstein, A. Vetter, B. V. Lahijani, H. P. Herzig, C. Rockstuhl, and M. S. Kim, "Inverse photonic design of functional elements that focus Bloch surface waves," Light Sci. Appl. **7**, 104 (2018).

19. U. Stella, L. Boarino, N. De Leo, P. Munzert, and E. Descrovi, "Enhanced directional light emission assisted by resonant Bloch surface waves in circular cavities," ACS Photonics **6**, 2073–2082 (2019).

20. T. Perani, D. Aurelio, and M. Liscidini, "Bloch-surface-wave photonic crystal nanobeam cavity," Opt. Lett. **44**, 5133–5136 (2019).

21. U. Stella, T. Grosjean, N. De Leo, L. Boarino, P. Munzert, J. R. Lakowicz, and E. Descrovi, "Vortex beam generation by spin-orbit interaction with Bloch surface waves," ACS Photonics **7**, 774–783 (2020).

22. K. R. Safronov, D. N. Gulkin, I. M. Antropov, K. A. Abrashitova, V. O. Bessonov, and A. A. Fedyanin, "Multimode interference of Bloch surface electromagnetic waves," ACS Nano **14**, 10428–10437 (2020).

23. M. Liscidini, "Surface guided modes in photonic crystal ridges: the good, the bad, and the ugly," J. Opt. Soc. Am. B **29**, 2103–2109 (2012).

24. T. Perani and M. Liscidini, "Long-range Bloch surface waves in photonic crystal ridges," Opt. Lett. **45**, 6534–6537 (2020).

25. Z. Zhu and T. G. Brown, "Full-vectorial finite-difference analysis of microstructured optical fibers," Opt. Express **10**, 853–864 (2002).

26. A. W. Snyder and J. D. Love, *Optical Waveguide Theory* (Chapman and Hall, 1991).

27. A. Taflove and S. Hagness, *Computational Electrodynamics: The Finite-Difference Time-Domain Method*, 3rd ed. (Artech House, 2005).

28. Q. Jiang, W. Li, C. Tang, Y. Chang, T. Hao, X. Pan, H. Ye, J. Li, and C. Gu, "Large scale fabrication of nitrogen vacancy-embedded diamond nanostructures for single-photon source applications," Chin. Phys. B **25**, 118105 (2016).

29. M. Häffner, A. Haug, A. Heeren, M. Fleischer, H. Peisert, T. Chassé, and D. P. Kern, "Influence of temperature on HSQ electron-beam lithography," J. Vac. Sci. Technol. B **25**, 2045–2048 (2007).

30. Y. Chen, K. Bi, Q. Wang, M. Zheng, Q. Liu, Y. Han, J. Yang, S. Chang, G. Zhang, and H. Duan, "Rapid focused ion beam milling based fabrication of plasmonic nanoparticles and assemblies via 'sketch and peel' strategy," ACS Nano **10**, 11228–11236 (2016).

31. N. Yao, *Focused Ion Beam Systems: Basics and Applications* (Cambridge University, 2007).

32. S. Reyntjens and R. Puers, "A review of focused ion beam applications in microsystem technology," J. Micromech. Microeng. **11**, 287–300 (2001).

33. F. S. Ligler, "Perspective on optical biosensors and integrated sensor systems," Anal. Chem. **81**, 519–526 (2009).

34. X. C. Yu, Y. Y. Zhi, S. J. Tang, B. B. Li, Q. H. Gong, C. W. Qiu, and Y. F. Xiao, "Optically sizing single atmospheric particulates with a 10-nm resolution using a strong evanescent field," Light Sci. Appl. **7**, 18003 (2018).